

Direct numerical simulation of stenotic flows, Part 1: Steady flow

By **SONU S. VARGHESE¹**, **STEVEN H. FRANKEL¹**
AND **PAUL F. FISCHER²**

¹School of Mechanical Engineering, Purdue University, 585 Purdue Mall, West Lafayette, IN 47907, USA

²Mathematics and Computer Science Division, Argonne National Laboratory, Argonne, IL 60439, USA

(Received 28 January 2005)

Direct numerical simulations (DNS) of steady and pulsatile flow through 75% (by area reduction) stenosed tubes have been performed, with the motivation of understanding the biofluid dynamics of actual stenosed arteries. The spectral-element method, providing geometric flexibility and high-order spectral accuracy, was employed for the simulations. The steady flow results are examined here while the pulsatile flow analysis is dealt with in Part 2 of this study. At inlet Reynolds numbers of 500 and 1000, DNS predicted a laminar flowfield downstream of an axisymmetric stenosis and comparison to previous experiments showed good agreement in the immediate post-stenotic region. The introduction of a geometric perturbation within the current model, in the form of a stenosis eccentricity that was 5% of the main vessel diameter at the throat, resulted in breaking the symmetry of the post-stenotic flowfield by causing the jet to deflect towards the side of the eccentricity and at a high enough Reynolds number of 1000, jet breakdown occurred in the downstream region. The flow transitioned into turbulence about five diameters away from the stenosis, with velocity spectra taking on a broadband nature, acquiring a $-5/3$ slope that is typical of turbulent flows. Transition was accomplished by the breaking up of streamwise, hairpin vortices into a localized turbulent spot, reminiscent of the turbulent puff observed in pipe flow transition, within which *r.m.s.* velocity and turbulent energy levels were highest. Turbulent fluctuations and energy levels rapidly decayed beyond this region and flow relaminarized. The acceleration of the fluid through the stenosis resulted in wall shear stress (WSS) magnitudes that exceeded upstream levels by more than a factor of thirty but low WSS levels accompanied the flow separation zones that formed immediately downstream of the stenosis. Transition to turbulence in the case of the eccentric stenosis was found to manifest itself in large temporal and spatial gradients of WSS, with significant axial and circumferential variations in the turbulent section.

1. Introduction

Atherosclerosis, a cardiovascular disease of the larger arteries, is the primary cause of heart disease and stroke. In the United States alone, statistics released by the American Heart Association estimated that more than 70 million Americans have one or more forms of cardiovascular disease, with coronary heart disease being the single leading cause of death, claiming almost 20% of all deaths in 2002 alone. Atherosclerosis is a progressive disease initiated by localized fatty streak lesions within the arteries occurring

as early as childhood. Over decades, these lesions can develop into more complex plaques large enough to significantly block blood flow within the circulatory system (Lusis 2000). This local restriction of the artery is known as an arterial stenosis. Plaque deposition is most common in the aorta, coronary arteries, and carotid arteries; and, as one might expect, the presence of a stenosis can lead to serious health risks. Stenoses are commonly characterized as a percentage reduction in diameter or area of the host vessel and are considered clinically significant when the reduction is greater than 75% by area (Young 1979; Ku 1997). The progression of a low-level arterial blockage into a critical stenosis is in itself the result of complex non-linear interactions between factors such as flow conditions, wall compliance, and biological responses (Berger & Jou 2000).

The cardiovascular system typically features low Reynolds number pulsatile flow due to the cyclic pumping motion of the heart. In particular, stenotic flows may feature flow separation, recirculation, and reattachment, as well as strong shear layers that, when combined with flow pulsatility, can result in periodic transition to turbulence in the post-stenotic region. Thus, the presence of a critical stenosis can reduce the flow rate through nonrecoverable head loss and flow choking. For example, a stenosis in one of the major vessels supplying the brain can choke the flow and lead to a cerebral stroke (Young 1979). The larger velocities at the stenosis as the flow accelerates through the occlusion, lead to high shear stresses at the stenosis throat (or neck,) which can activate platelet accumulation and induce thrombosis, leading to plaque rupture and complete blockage of the vessel. Low, oscillatory shear stresses in the disturbed flow regions have been directly implicated in the progression of arterial wall thickening and atherosclerotic disease (Ku 1997; Wootton & Ku 1999). Understanding the complex flow features that occur in the vicinity of a stenosis is thus critical to understanding the possible mechanisms by which induced flow dynamics can contribute to disease progression.

1.1. Pulsatile turbulent wall-bounded flow

In the most idealized sense, a stenosed vessel resembles a straight rigid pipe with a constriction. A number of works have focussed on the topic of unsteady turbulent pipe flows, including periodic pulsating flows and non-periodic transient flows. The fundamental variables involved in pulsatile flows are the amplitude and frequency of the pulsatile wave and the mean flow rate. Several studies have shown that the effect of amplitude on velocity and turbulence is small, while that of the pulsating frequency and mean flow rate can be significant (He & Jackson 2000).

Winter & Nerem (1984) reviewed pulsatile flows and qualitatively classified them in three types: (a) laminar flow, which exists throughout the cycle with no disturbances at any time; (b) periodic generation of turbulence, which arises when high-frequency velocity fluctuations appear at the beginning of the decelerating phase of the flow cycle, decrease in intensity as mean flow velocity decreases, and dissipates as the flow relaminarizes at the beginning of the subsequent acceleration phase; and (c) fully turbulent flow, which occurs throughout the cycle. More recently, He & Jackson (2000) provided a thorough review of the literature dealing with turbulence in transient pipe flow. Their study of the same subject yielded valuable insight on some fundamental aspects of turbulence dynamics. They observed that turbulence intensity is attenuated in accelerating flows and increased in decelerating flows mainly because of the delayed response of turbulence production, a delay in turbulent energy redistribution among its three components, and a delay associated with the radial propagation of turbulence.

Scotti & Piomelli (2001a) conducted direct numerical simulations (DNS) and large eddy simulations (LES) of pulsating flow in a channel at different frequencies and examined the time-dependent characteristics of the flow as well as the distribution of instantana-

neous coherent structures, which were found to be phase dependent. At low frequencies, more relevant for the physiologic flows motivating the present study, the flow contained very little turbulent kinetic energy at the beginning of the acceleration phase but eventually developed long, smooth streaks that burst into a turbulent spot towards the end of acceleration. The localized spot was found to spread to the entire flow during the deceleration phase. Scotti & Piomelli (2001b) also employed the Reynolds averaged Navier-Stokes (RANS) equations to assess the capabilities of different turbulence models in predicting the same flow. The RANS approach involves computation of only the mean flow, with the effects of the turbulent eddies being modeled. The velocity profiles computed by the turbulence models over the course of a cycle agreed well with the DNS and LES profiles, but differences in other turbulence quantities were noted.

1.2. *Experimental stenotic flow studies*

Because of the obvious limitations of conducting *in vivo* measurements of flow in stenosed arterial vessels, several *in vitro* studies have been performed to study the post-stenotic flowfield. In a majority of these studies, factors such as wall compliance, non-Newtonian fluid behavior, and the constituent particles in blood have been neglected, being regarded as of secondary importance in most physiological stenotic flows (Ku 1997).

Giddens and coworkers have made extensive laser Doppler anemometry measurements of stenotic flows using plexiglass models of axisymmetric stenotic vessels, under conditions of both steady and pulsatile inflow (Cassanova & Giddens 1978; Deshpande & Giddens 1980; Khalifa & Giddens 1981; Ahmed & Giddens 1983a,b, 1984; Lieber & Giddens 1988, 1990). For steady flow at low Reynolds numbers of about 500, the post-stenotic flowfield contained only disturbances associated with discrete frequency vortex shedding. Transition to turbulence was restricted to models with a stenosis degree higher than 75% (by area), at Reynolds numbers greater than 1000 (Ahmed & Giddens 1983a,b). In the case of pulsatile flow at a physiologically relevant mean (cycle-averaged) inlet Reynolds number of 600, a start-up coherent vortex structure was produced at the beginning of each cycle and was accompanied by discrete frequency, laminar oscillations that amplified during the early stages of flow deceleration in the immediate post-stenotic region; but the flow remained stable for mild constrictions of degree 50% or less. For the clinically significant 75% stenosis, unstable discrete frequency velocity oscillations evolved into turbulence during the deceleration phase and interacted with the starting structure (Ahmed & Giddens 1984). From here on, all stenosis degrees are expressed in terms of percentage area reduction.

In a later work, Ojha *et al.* (1989) studied pulsatile flow through constricted tubes using photochromic tracer methods. They observed that with occlusions of less than 50%, isolated regions of vortical structures were found in the vicinity of the reattachment point, primarily during the deceleration phase. For tighter constrictions, transition to turbulence was triggered just prior to peak flow, attributed to the breakdown of streamwise vortices shed in the shear layer. Other noteworthy experimental studies of stenotic flows within the past three decades include the work of Kim & Corcoran (1974), Fredberg (1974), Young & Tsai (1979a,b), Clark (1980), Lu *et al.* (1980, 1983), and Abdallah & Hwang (1988).

1.3. *Computational modeling of stenotic flows*

In the past decade or so, computational fluid dynamics (CFD) has begun to play a major role in studying arterial flows and stenotic flows in particular. CFD studies have considered both steady and pulsatile stenotic flows, coupled with fluid structure interactions, non-Newtonian effects, and flow in geometries reconstructed from clinical magnetic res-

onance imaging measurements (Tang *et al.* 1999; Bathe & Kamm 1999; Buchanan Jr. *et al.* 2000; Stroud *et al.* 2000).

The various stenotic flow experiments listed in § 1.2 confirmed the presence of highly disturbed flow downstream of a stenosis and even transition to turbulence in the presence of stenoses greater than 75%. However, simulating turbulent flows in complex geometries involves overcoming several numerical obstacles, such as sufficient mesh resolution required to simulate all the scales of turbulence. At the same Reynolds number, it can be even more difficult to simulate transition to turbulence as opposed to fully turbulent flow because of the presence of localized small-scale structures that are transported with minimum physical dissipation, requiring sufficient spatial resolution and accurate long-time integration (Fischer, Kruse & Loth 2002).

With the exception of the numerical studies by Mallinger & Drikakis (2002), Mittal, Simmons & Najjar (2003), and Sherwin & Blackburn (2004), most stenotic flow simulations have been conducted in the laminar regime, failing to address the issue of turbulence in the post-stenotic field. The unsteady RANS predictions of pulsatile stenotic flows performed by Varghese & Frankel (2003) highlight the inability of traditional turbulence models to accurately predict all the complex flow features reported by experimentalists downstream of a stenosis. Recently, Ryval, Straatman & Steinman (2004) were able to obtain much improved RANS predictions for the same flows using improved inlet boundary conditions, in the form of the Womersley solution for laminar, pulsatile flow through rigid tubes (Womersley 1955). While some promise for simulating physiological flows using simple two-equation turbulence models has been demonstrated, these models are yet to be validated against detailed measurements of transitional and turbulent post-stenotic flow that can only be carried out via DNS or LES.

Mallinger & Drikakis (2002) conducted high-order simulations of instabilities in pulsatile flow through a three-dimensional axisymmetric stenosis, revealing the existence of flow instabilities throughout the pulsatile cycle that are manifested by highly asymmetric flow and helical disturbances downstream of the stenosis. Mittal *et al.* (2003) performed LES of pulsatile flow through a planar channel with a one-sided semicircular constriction and also found evidence of transition to turbulence in the downstream section. In both these studies a small, white-noise, random perturbation was imposed on all components of the inflow velocity to break the flow symmetry. Most recently, Sherwin & Blackburn (2004) conducted stability analyses of steady and pulsatile, axisymmetric stenotic flows. They found that steady flow undergoes a Coanda-type wall attachment and turbulent transition through a subcritical bifurcation, while pulsatile flows become unstable through a subcritical period-doubling bifurcation involving alternating tilting of vortex rings that are ejected from the throat with each pulse and rapidly break down through a self-induction mechanism. Localized transition, followed by relaminarization further downstream, was observed at the physiologically realistic Reynolds numbers employed in their study.

1.4. *The present study*

The goal of the present study is to thoroughly detail, through direct numerical simulations, the instantaneous and statistical flow features that occur downstream of a stenosis under both steady and pulsatile inflow conditions, complementing the information yielded by previous numerical studies. This idealized study has been conducted in terms of non-dimensional parameters to provide a fundamental basis for understanding the flow dynamics that may be generated by even more complex occlusions within the arterial tree. For the simulations, we used the spectral-element method, which allows for geometric flexibility and nonconforming meshes for local refinement, while providing high-order

accuracy. To maintain the physiologic relevance of the study and allow for validation, we stayed as close as possible to the classical stenotic flow experiments of Ahmed & Giddens (1983a, 1984). As in the experiments, the effect of wall compliance and non-Newtonian effects have been ignored. Because of the symmetry of the stenosis model about the main vessel axis, a geometric perturbation in the form of an eccentricity was introduced at the stenosis throat to produce asymmetries and disturbed flow in the post-stenotic region. This is extremely relevant even in the physiologic sense because actual arterial stenoses are highly unlikely to exhibit any axisymmetry (Stroud *et al.* 2000).

The results obtained under steady inflow conditions are presented in this paper, while the pulsatile flow details are covered in Part 2 (Varghese, Frankel & Fischer 2005). The flow model and numerical method are detailed in § 2. Results and discussion, including comparison with experiments for the steady inflow case, are presented in § 3. Conclusions follow in § 4.

2. Problem formulation

Steady flow through both axisymmetric and eccentric stenotic flow models were studied, with both stenosis geometries corresponding to a maximum area restriction of 75% at the throat. The baseline stenosis geometry modeled for this study was similar to that used in the stenotic flow experiments of Ahmed & Giddens (1983a, 1984) and is described in § 2.1. The numerical methodology employed for all the simulations reported here is outlined in § 2.2.

2.1. Flow model and dimensionless groups

Profiles of the axisymmetric and eccentric stenosis models are shown in figure 1. A cosine function dependent on the axial coordinate, x , was used to generate the shown geometry. The cross-stream coordinates, y and z , were computed by using $S(x)$, specifying the shape of the stenosis as

$$\begin{aligned} S(x) &= \frac{D}{2} [1 - s_o (1 + \cos (\frac{2\pi(x-x_o)}{L}))], \\ y &= S(x) \cos \theta, \\ z &= S(x) \sin \theta, \end{aligned} \quad (2.1)$$

where D is the diameter of the non-stenosed tube, $s_o = 0.25$ for the 75% area reduction stenosis used throughout this study, L is the length of the stenosis ($= 2D$ in this study), and x_o is the location of the center of the stenosis ($x_o - \frac{L}{2} \leq x \leq x_o + \frac{L}{2}$).

For the eccentric model, the stenosis axis was offset from the main vessel axis by $0.05D$. The offset, $E(x)$, and subsequently the modified y and z coordinates were computed as

$$\begin{aligned} E(x) &= \frac{s_o}{10} (1 + \cos (\frac{2\pi(x-x_o)}{L})), \\ y &= S(x) \cos \theta, \\ z &= E(x) + S(x) \sin \theta. \end{aligned} \quad (2.2)$$

As equation (2.2) shows, the offset was introduced in the $x-z$ plane corresponding to $y = 0.0$ only. In both models, the upstream and downstream sections of the vessel extended for three and sixteen vessel diameters, respectively, as measured from the stenosis throat (located at $x = 0$ in the figure).

For the steady flow simulations, the parabolic velocity profile for laminar, fully developed Poiseuille flow was imposed at the inlet as

$$\frac{u}{u_m} = 2(1 - r^2), \quad (2.3)$$

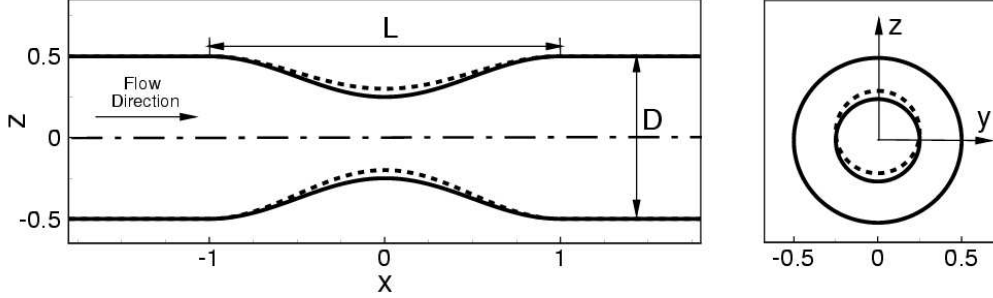


FIGURE 1. Side and front views of the stenosis geometry ($L = 2D$), the solid line corresponding to the profile of the axisymmetric model and the dashed line to the eccentric model; x is the streamwise direction while y and z are the cross-stream directions. The front view shows the cross-section corresponding to both models in the main vessel and at the throat, $x = 0.0$.

where u_m is the cross-sectional averaged inlet velocity and $r = \sqrt{y^2 + z^2}$ is the radial distance from the vessel centerline.

The vessel walls were assumed to be rigid for all simulations within this study, with the no-slip boundary condition applied at the walls. All parameters and normalizations used here were chosen to match the flow conditions in the experiments by Ahmed & Giddens (1983a) to facilitate comparisons with their measurements. The simulations through the axisymmetric and eccentric stenoses models were both performed at Reynolds numbers of 500 and 1000, based on the vessel diameter D and mean inlet velocity u_m .

2.2. Numerical methodology

The numerical simulations employed a spectral-element code, developed at Argonne National Laboratory, that is especially suited for simulation of transitional and turbulent flows in complex geometries, and is described by Fischer *et al.* (2002). The code is based on the nonconforming spectral element method (SEM) for solution of the incompressible Navier-Stokes equations in \mathbb{R}^d (here, $d = 3$),

$$\begin{aligned} \frac{\partial \mathbf{u}}{\partial t} + \mathbf{u} \cdot \nabla \mathbf{u} &= -\nabla p + \frac{1}{Re} \nabla^2 \mathbf{u} \quad \text{in } \Omega, \\ \nabla \cdot \mathbf{u} &= 0 \quad \text{in } \Omega, \end{aligned} \quad (2.4)$$

where $\mathbf{u} = (u, v, w)$ is the velocity vector, p is the pressure, and $Re = UL/\nu$ is the Reynolds number based on a characteristic velocity, length scale, and kinematic viscosity. The associated initial and boundary conditions are,

$$\begin{aligned} \mathbf{u}(\mathbf{x}, 0) &= \mathbf{u}^0(\mathbf{x}), \\ \mathbf{u} &= \mathbf{u}_v \quad \text{on } \partial\Omega_v, \\ \nabla u_i \cdot \hat{\mathbf{n}} &= 0 \quad \text{on } \partial\Omega_o, \end{aligned} \quad (2.5)$$

where $\hat{\mathbf{n}}$ is the outward pointing normal on the boundary and subscripts v and o indicate boundary regions where Dirichlet velocity or Neumann outflow boundary conditions are specified, respectively.

Temporal discretization of the Navier-Stokes equations (2.4) was based on the high-order operator-splitting methods developed by Maday, Patera & R nquist (1990). This approach separates the linear viscous term from the non-linear advection contribution. Time integration of the advection term was advanced quickly by using an explicit scheme, while the linear symmetric Stokes problem was solved implicitly. Third-order accurate time-stepping was employed for all the simulations except in the case of pulsatile flow

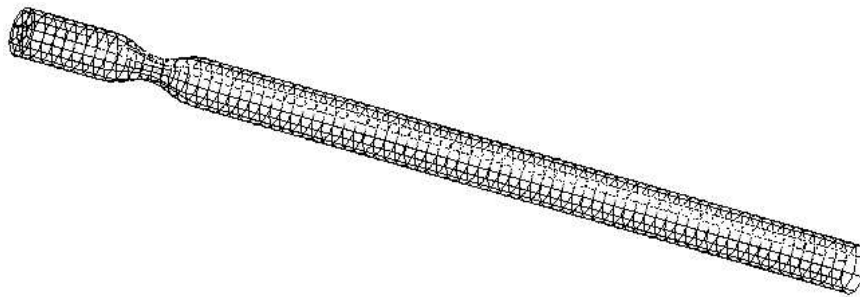


FIGURE 2. Representative mesh employed for the axisymmetric model simulations. The mesh comprises $K = 1600$ hexahedral cells.

through the eccentric stenosis, for which time-stepping was of the second-order, owing to the better stability properties of the latter (Deville, Fischer & Mund 2002). The solution was further stabilized by using the filter developed by Fischer & Mullen (2001).

The spatial discretization was based on the $P_N - P_{N-2}$ spectral-element method, which represents velocity (N) and pressure ($N - 2$) as N th-order tensor product Lagrange polynomials, based on Gauss or Gauss-Lobatto (GL) quadrature points, within each of K computational mesh cells. The total number of gridpoints is approximately KN^3 . SEM couples the efficiency of global spectral methods with the geometric flexibility of finite elements provided by nonconforming, deformed hexahedral elements. A representative mesh employed for the axisymmetric model simulations and comprising $K = 1600$ hexahedral cells is shown in figure 2. The method provided accurate solutions with minimal numerical dissipation and dispersion. Further details on the discretization and solution procedure, along with temporal and spatial convergence results, can be found in the literature (Fischer 1997; Deville *et al.* 2002).

2.2.1. Outflow boundary condition treatment

In turbulent flows, it is possible to have vortices strong enough to yield a (locally) negative flux at the outflow boundary. Since no flow characteristics are specified on these boundaries, this condition typically leads to instabilities with catastrophic results. One way to ensure that the characteristics are always pointing outwards is to force the flow through a nozzle, which effectively adds a constant to the outward normal component of the velocity field.

This nozzle effect can be imposed numerically without having to change the mesh geometry by imparting a positive divergence to the flow field near the exit. In the current study, this is done by identifying the layer of elements adjacent to the outflow and imposing a divergence function $D(x)$ that is zero at the end of the element away from the boundary and that ramps to a fixed value as one approaches the outflow boundary.

The results of this fix are illustrated by the velocity vector plots shown in figure 3, obtained along a plane passing through the main vessel axis close to the outflow for steady flow through the eccentric stenosis at a Reynolds number of 1000. Figure 3 (a) shows the flow field computed with the outflow correction. The flow is indeed leaving the domain at all points along the outflow boundary. The center panel, figure 3 (b), shows the uncorrected case, which has flow coming into the outflow boundary and which becomes catastrophically unstable within 100 time-steps beyond this point. The rightmost panel, figure 3 (c), shows that the difference between these two cases is indeed restricted to the outflow region, $x > 15.5D$. That is, the outflow treatment does not pollute the solution

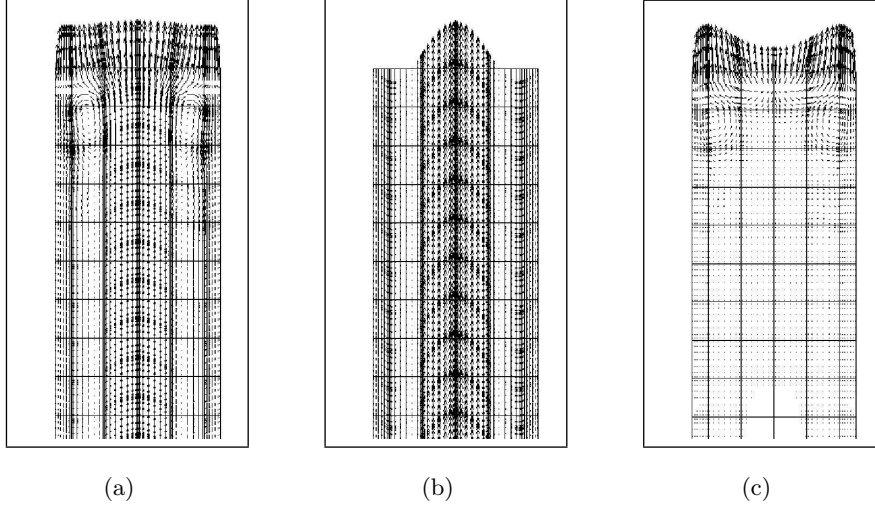


FIGURE 3. Velocity vector plots near the outflow for steady flow through the 75% eccentric stenosis at $Re = 1000$. (a) Corrected case, (b) uncorrected case, and (c) the difference between the two.

far upstream of the boundary. This was observed to be the case in all the simulations performed for this study.

2.3. Data reduction

We define here the averaging operations employed in this study. Under conditions of steady inlet flow, for a generic flow variable f , the time-averaged mean over a period of time T_f is computed as

$$\bar{f}(x, y, z) = \frac{1}{T_f} \int_{t_0}^{t_0 + T_f} f(x, y, z, t) dt, \quad (2.6)$$

where t_0 is the time at which the averaging process is initiated. The deviation from this average, which represents the random turbulent fluctuations, is then defined as

$$f'(x, y, z, t) = f(x, y, z, t) - \bar{f}(x, y, z). \quad (2.7)$$

Root mean square (*r.m.s.*) quantities are subsequently computed as

$$f'_{r.m.s.} = \sqrt{\overline{f'^2}}. \quad (2.8)$$

2.4. Grid independence and simulation details

Numerical convergence studies performed for the case of steady flow through the axisymmetric stenosis confirmed that the spatial resolution was sufficient. Figure 4 compares axial velocity profiles obtained by using a mesh with $K = 1600$ hexahedral cells and polynomial order of $N = 9$ and a mesh with $K = 2400$ and $N = 9$, a 50% increase in the number of gridpoints. The results obtained with the two computational meshes agree very well with each other, and so the $K = 1600, N = 9$ mesh was deemed sufficient for the axisymmetric model simulations. The resolution was increased by increasing the polynomial order to $N = 12$ for the eccentric model simulations, and this was determined to be adequate.

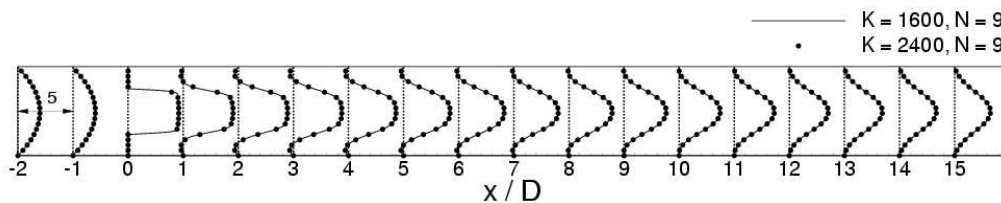


FIGURE 4. Comparison of axial velocity profiles for steady flow through the 75% axisymmetric stenosis model at $Re = 500$ for two grid sizes, with $K = 1600$ and $K = 2400$. The polynomial order $N = 9$ in both cases.

In the case of the axisymmetric stenosis model, the initial conditions for the steady flow simulations were set by starting the computations with typically large viscosity ($Re \approx 10$). The viscosity was subsequently lowered after a few thousand time-steps while simultaneously increasing the inlet velocity to ultimately match the Reynolds numbers considered here, $Re = 500$ and 1000 . Steady-state (time-invariant) results from these simulations were employed as initial conditions for the corresponding eccentric model computations. All the results presented in the following sections were obtained after confirming that initial transients had left the computational domain. Non-dimensional time-step sizes of $1.0e-3$ and $5.0e-4$ were used for the axisymmetric and eccentric cases, respectively. On 32 processors of an AMD Athlon based Linux cluster, computing times ranged from a day to ten days, depending on the computational complexity of the simulation, in terms of grid size and time-step requirements.

3. Results and discussion

3.1. Axisymmetric model

Axial velocity and vorticity magnitude contours in figure 5 show a laminar axisymmetric jet and shear layer for the 75% axisymmetric stenosis with an inlet Reynolds number of 500. The fluid accelerates through the constriction creating a plug-like velocity profile within the stenosis and a flow separation region immediately downstream. The peak velocities in the immediate downstream section exceed the mean inlet velocity (u_m) by more than a factor of four. Axial velocity profiles at five axial stations downstream of the stenosis are compared with digitized experimental results made by Ahmed & Giddens (1983a) in figure 6. In order to highlight the sensitivity of the stenosis degree on flow physics, profiles computed for models with area reductions of 70% and 73% are also shown, the stenosis length being kept constant at $2D$ throughout. The profiles predicted for the 73% model match exactly with the experiments immediately downstream of the stenosis, at locations $x = 1D$ and $2.5D$. Further downstream the agreement veers off, especially close to the wall, where absolute differences between the numerics and experiments are as large as 20%. The experimental profiles in this region are considerably fuller than their computed counterparts, with the size of the separation zone reducing with axial distance and flow completely reattaching to the wall between $x = 4D$ and $6D$, suggesting that the flow is not completely laminar. In the current simulation, however, separation continues well beyond this location, with the flow downstream of the 75% stenosis reattaching at $x \approx 10D$, as shown in figure 4. The flow maintains its jet-like character even as far as $x = 15D$, with peak velocity at this location attaining values more than three times the mean, 50% larger than the $2u_m$ peak velocity for the inlet Poiseuille solution.

The downstream flow field predicted here is laminar and axisymmetric with no evidence

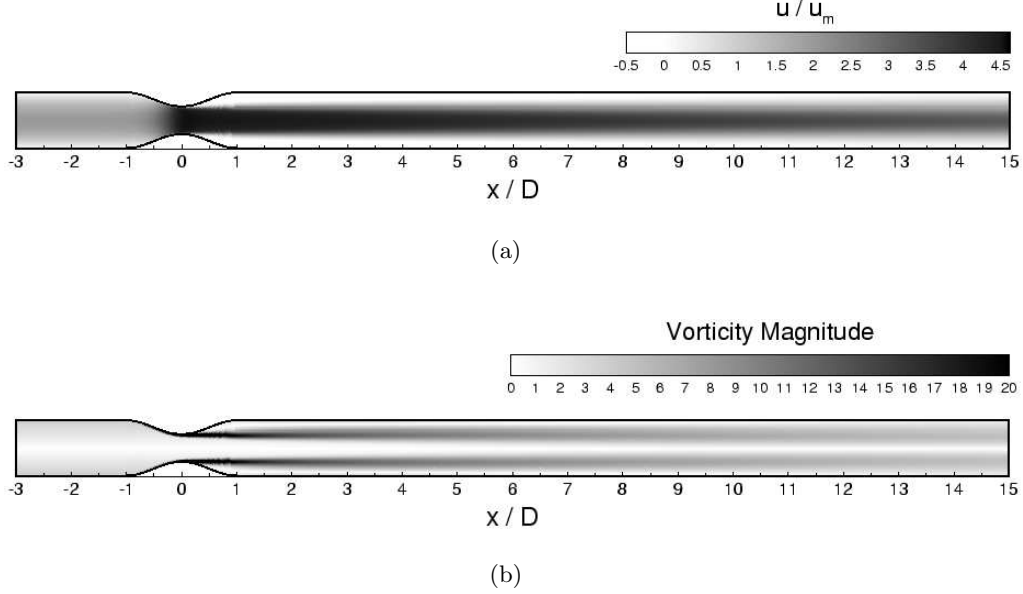


FIGURE 5. Contour plots for steady flow through the 75% axisymmetric stenosis at $Re = 500$. (a) Axial velocity, normalized by u_m , and (b) vorticity magnitude, normalized by u_m/D . Similar normalizations are employed in all subsequent presentations of steady flow results.

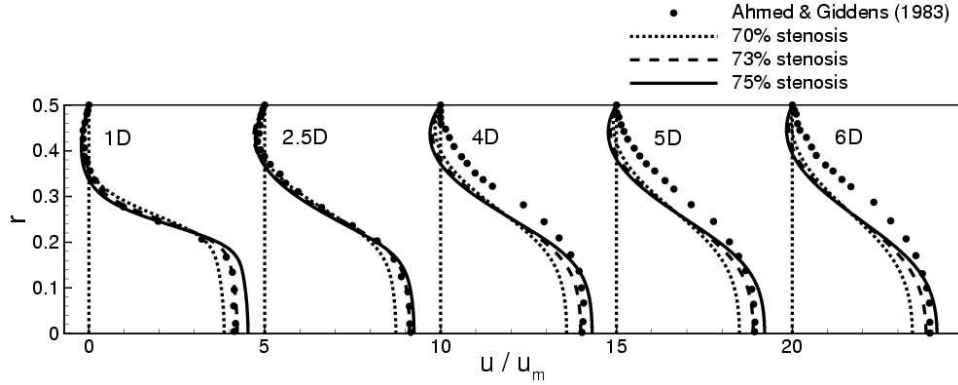
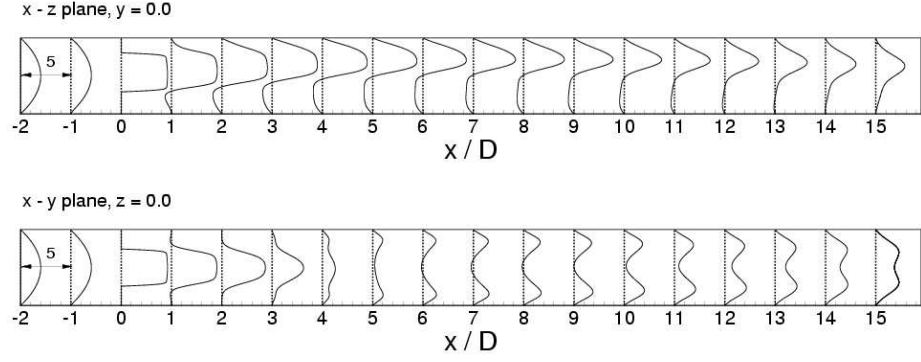


FIGURE 6. Comparison of axial velocity profiles at downstream locations with experimental profiles for steady flow through the axisymmetric stenosis at $Re = 500$. The axial stations are indicated in terms of diameters downstream from the stenosis throat.

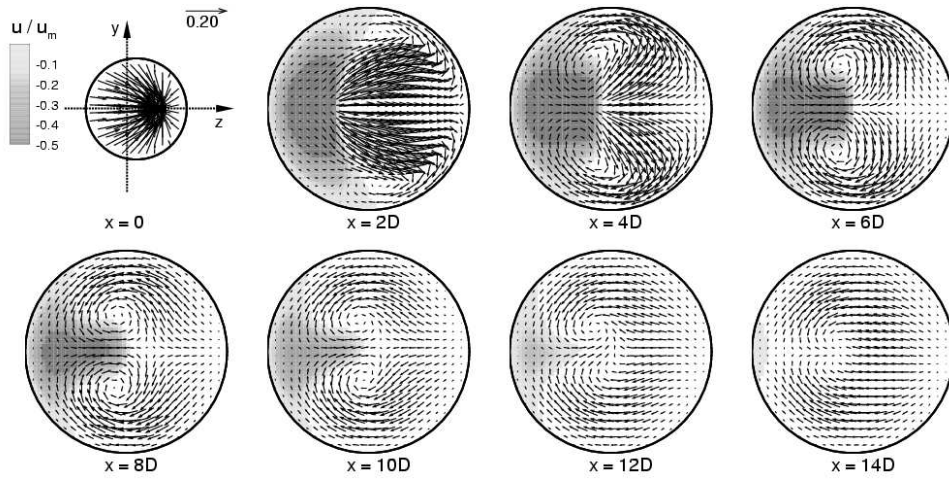
of jet breakdown and shear layer oscillation. A very similar flow field is predicted for the $Re = 1000$ case, and results are not shown here because the velocity and vorticity magnitude contours are qualitatively similar to those in figure 5.

3.2. Eccentric model

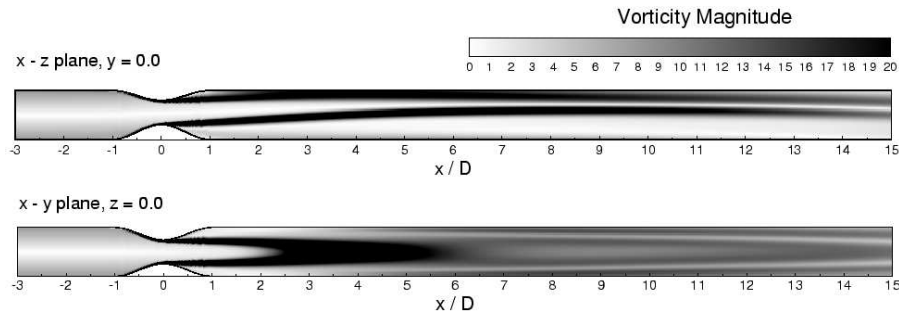
At an inlet Reynolds number of 500, the velocity and vorticity results in figure 7 illustrate the effect of a $0.05D$ eccentricity at the stenosis throat. Axial velocity levels above 0.0 have been blanked out in figure 7 (b) to highlight reverse flow regions. While the streamwise



(a)



(b)



(c)

FIGURE 7. Steady flow through the 75% eccentric stenosis at $Re = 500$. (a) Axial velocity profiles, (b) in-plane velocity vectors superimposed on axial velocity contours at downstream stations (the dark regions indicate negative velocity, i.e. into the page), and (c) vorticity magnitude contours.

velocity in the stenosis exhibits the same plug-shaped profile as in the axisymmetric model, with peak velocity greater than $4u_m$, the in-plane velocity vectors show that strong crossflow velocities, created by the geometric perturbation, deflect the jet toward the side of the eccentricity. The biasing of the stenotic jet is clearly highlighted by the velocity profiles and vorticity magnitude contours in the plane of eccentricity (corresponding to $y = 0.0$). The accelerating jet causes flow separation along the side of the vessel that is farther away from the stenosis, forming a rather large recirculation region that covers almost half the vessel section at $x = 2D$, as indicated by the dark-shaded region in figure 7 (b). Further downstream, the crossflow velocity vectors are deflected along the walls and form a pair of weak counter-rotating vortices along the edge of the recirculation region. These entrain more fluid from the jet into the recirculation zone, causing it to recede along the walls, while extending farther into the vessel core. Flow separation extends as far as the centerline in the region between $x = 6D$ and $8D$. At this point, the jet is deflected by the wall back toward the vessel center, causing the recirculation zones to recede. Complete flow reattachment occurs only after $x \approx 14D$.

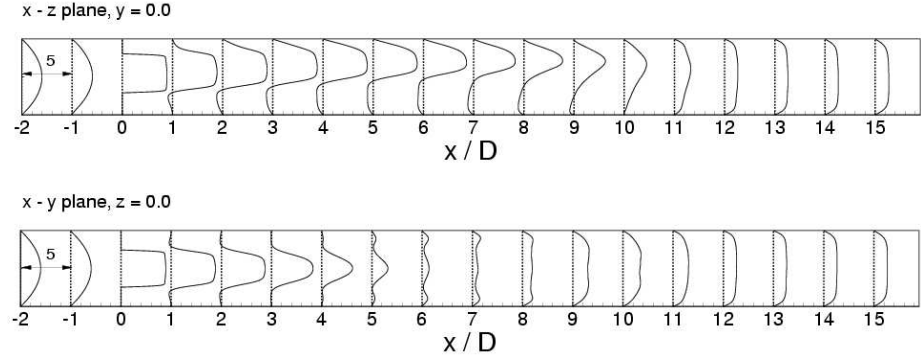
Figure 7 (a) shows that the movement of the jet and the recirculation region is symmetric about the $z = 0.0$ plane, which bisects the tube perpendicular to the plane of eccentricity. Note that the stenosis is also symmetric about this plane. The initial biasing of the jet away from the $z = 0.0$ plane is clear, resulting in lower velocities along the vessel centerline as the recirculation zone creeps up toward the core. With the jet being directed back to the center after $x = 8D$ and centerline velocities once again starting to increase, the profiles begin to acquire a more uniform shape in this plane. However, in the $y = 0.0$ plane, the flow continues to maintain its jet-like character in the far downstream region, as shown in the velocity profile and vorticity plots. The profiles in this plane tend more toward those predicted for the axisymmetric model, with peak velocities about $3u_m$ at $x = 14D$. The results suggest that the flow will eventually resemble a weak elliptic jet far downstream of the stenosis throat, one whose major axis is aligned with the $z = 0.0$ plane, before reverting to the parabolic inlet profile. At this Reynolds number, however, the flow is essentially laminar across the entire post-stenotic region, with no evidence of flow disturbances.

3.2.1. Transition to turbulence: evolution of averaged flow characteristics

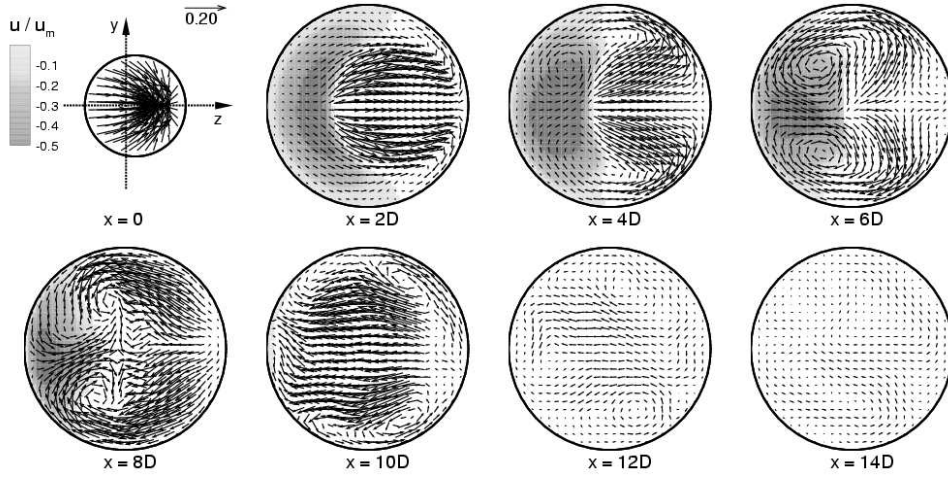
Unlike the axisymmetric cases, when the inlet Reynolds number is increased to 1000 for the eccentric model, the flow characteristics in the post-stenotic region alter considerably, with localized transition occurring after approximately $x = 4D$. The time-averaging operation defined in equation (2.6) was employed for this case over a non-dimensional time $T_f u_m / D = 100$ and the time-averaged results are presented in figure 8.

Velocity profiles in both the vessel bisecting planes and in-plane vectors closely match those seen at $Re = 500$ until about $x = 3D$. The stenotic jet is deflected toward the wall along the side of the eccentricity, creating a distinct crescent-shaped recirculation zone along the opposite side. As at the lower Reynolds number, the crossflow velocities at $x = 2D$ are deflected by the wall and reduce the extent of the recirculation region along the walls, at the same time pushing it up to the centerline. Farther downstream, the differences between this simulation and its low Reynolds number counterpart become readily apparent upon comparing the corresponding recirculation zones, namely, the dark-shaded regions of figures 7 (b) and 8 (b), in which positive axial flow regions have been blanked out.

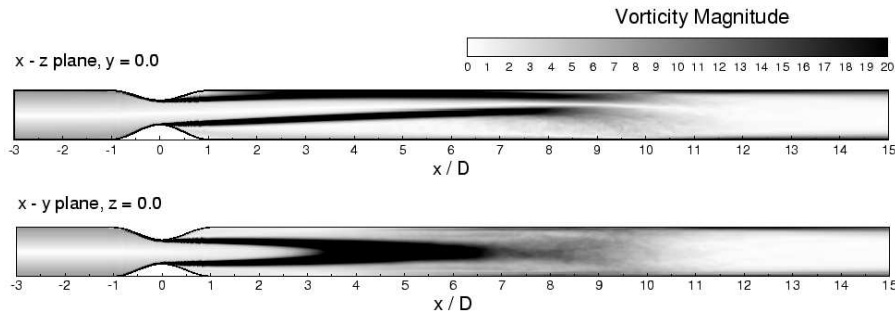
At $Re = 1000$, almost half the cross-section experiences negative velocities in the vicinity of the $x = 4D$ station. The stenotic jet starts to breakdown after $x = 6D$, as the jet is deflected back toward the center. The relatively large crossflow velocities in



(a)



(b)



(c)

FIGURE 8. Time-averaged results for steady flow through the 75% eccentric stenosis at $Re = 1000$. (a) Axial velocity profiles, (b) in-plane velocity vectors superimposed on axial velocity contours at downstream stations (the dark regions indicate negative velocity, i.e. into the page), and (c) vorticity magnitude contours.

this region (as compared with those between $x = 6D$ and $10D$ at $Re = 500$) push the recirculation region back along the walls until it recedes completely within the length of a few vessel diameters. As evidenced by the velocity profiles in figure 8(a), the flow fully reattaches by $x \approx 10D$, almost four vessel diameters earlier than the low Reynolds number case. Vorticity magnitude contours in figure 8 (c) confirm complete breakdown of the jet and shear layer by $x = 11D$. In the far downstream section, $x \geq 11D$, the velocity differential across the vessel section disappears, and axial velocity profiles take on a uniform shape that is more typical in turbulent flows, with peak velocities close to $1.5u_m$.

3.2.2. Turbulent statistics

The intensity of any turbulent flow can be gauged by studying the *r.m.s.* velocities, $\sqrt{u'^2}$, $\sqrt{v'^2}$, and $\sqrt{w'^2}$, defined in § 2.3. The three normal Reynolds stress components, $\overline{u'^2}$, $\overline{v'^2}$, and $\overline{w'^2}$ are a measure of the kinetic energy per unit mass of the velocity fluctuations in each of the coordinate directions, and the turbulent kinetic energy, or the kinetic energy of the turbulent fluctuations per unit mass, can in turn be defined as $k = \frac{1}{2}\overline{u'_i u'_i}$ (Tennekes & Lumley 1972; Wilcox 1993).

Streamwise and cross-stream *r.m.s.* velocity profiles are shown in figure 9, with mean inlet velocity u_m used for non-dimensionalization. In both planes the streamwise *r.m.s.* velocity $u_{r.m.s.}/u_m$ is amplified as one moves farther away from the stenosis throat, especially after $x = 4D$ where peak values, $(u_{r.m.s.})_{max}$, are almost 50% of u_m . At axial stations preceding $x = 7D$, peak *r.m.s.* levels occur along the shear layer. However, as the shear layer breaks up in the region $x > 6D$ the turbulent energy is redistributed across the entire cross-section of the vessel. This is also clear from the distribution of turbulent kinetic energy profiles in the post-stenotic region, shown in figure 10. These profiles are non-dimensionalized by u_m^2 and qualitatively match the streamwise *r.m.s.* velocity profiles at each axial location. The peaks in the profiles immediately downstream of the stenosis show that turbulent energy is concentrated in the shear layer, indicating that the instability initially propagates along the shear layer. Only after $x \approx 6D$ do the profiles tend to a more uniform nature, as a result of turbulent jet breakdown and disturbances rapidly diffusing over the cross-section, smearing the peaks with increasing axial distance. Turbulent kinetic energy and $u_{r.m.s.}$ attain maximum levels in the turbulent region between $x = 6D$ and $x = 10D$, with $(u_{r.m.s.})_{max} \approx 1.2u_m$ at $x = 9D$. After the flow has completely reattached at $x = 10D$, streamwise *r.m.s.* velocity profiles acquire a more uniform shape, but levels drop from about $0.5u_m$ at $x = 11D$ to less than $0.2u_m$ at $x = 15D$ as viscous effects dominate and the flow relaminarizes. Correspondingly, the turbulent energy attenuates after $x = 11D$, eventually decaying to almost negligible levels close to the outflow.

Profiles of $v_{r.m.s.}$ and $w_{r.m.s.}$ in figure 9 show that the cross-stream turbulent velocities follow the trend of the streamwise turbulent velocity profiles, with sharp amplification occurring after $x = 4D$. Peak values in this region are approximately $0.1u_m$ and increase to about $0.3u_m$ as the shear layer starts to break up at around $x \approx 6D$. The subsequent breakdown region experiences the highest levels of turbulent energy generated by these cross-stream velocity fluctuations, with peak values rising to almost $0.6u_m$ at $x = 9D$. Further downstream, as seen in the streamwise *r.m.s.* data, $v_{r.m.s.}$ and $w_{r.m.s.}$ tend to become more evenly distributed across the vessel section while their magnitude keeps dropping, eventually falling to approximately $0.1u_m$ at $x = 15D$. Comparing the streamwise and cross-stream turbulent velocities, one sees that immediately downstream of the stenosis most of the turbulent kinetic energy is siphoned off to the streamwise

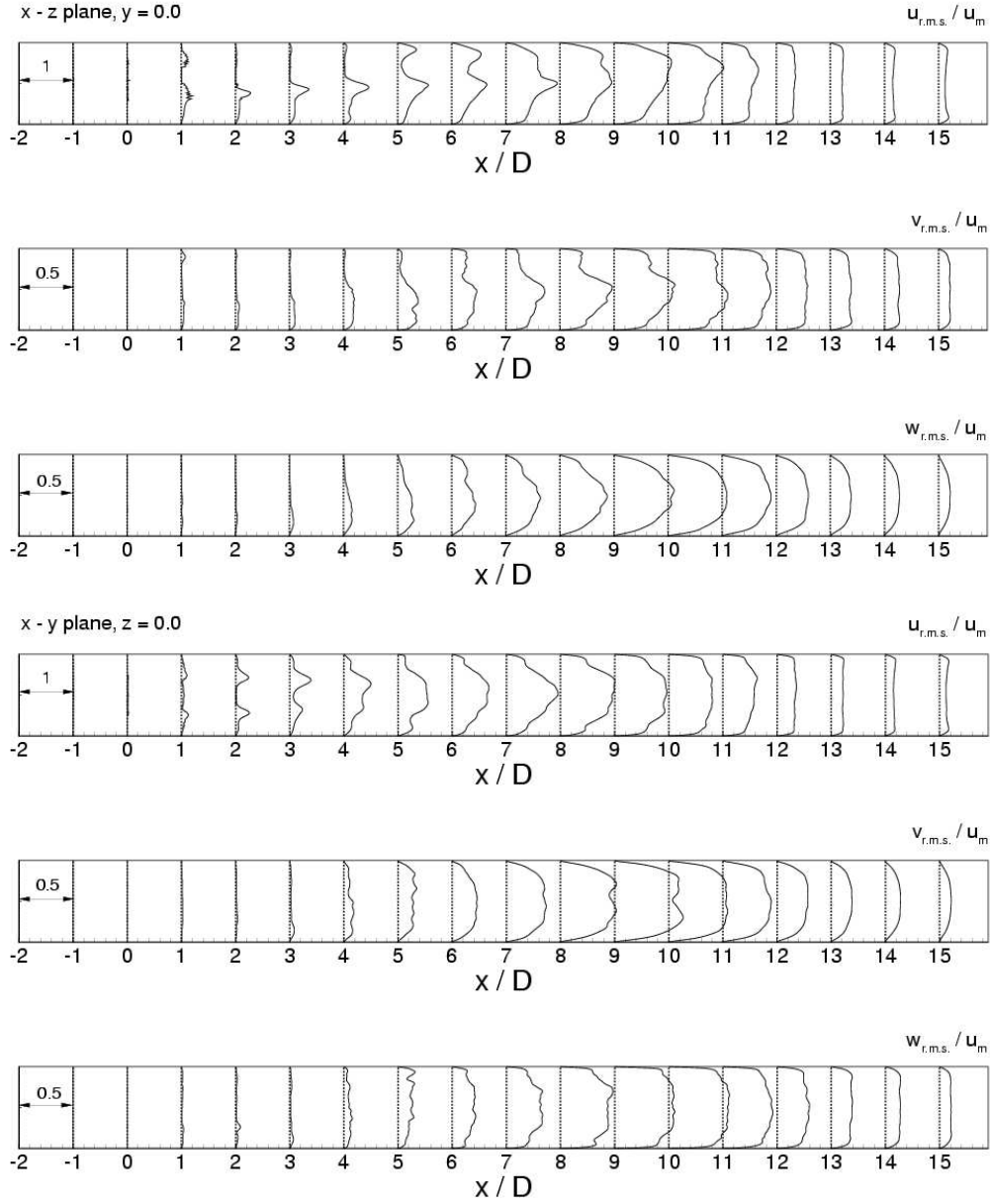


FIGURE 9. *R.M.S.* velocity profiles, normalized by mean inlet velocity u_m , for steady flow through the 75% eccentric stenosis at $Re = 1000$.

fluctuations before being redistributed to the other components by $x = 11D$, with $u_{r.m.s.}$ almost always 50% larger than both $v_{r.m.s.}$ and $w_{r.m.s.}$ across the entire turbulent section. This also indicates that turbulent breakdown is non-isotropic, an observation made by Deshpande & Giddens (1980) in their study of steady flow through a 75% axisymmetric stenosis (similar to the one used in this study), albeit at a much higher Reynolds number of 15000.

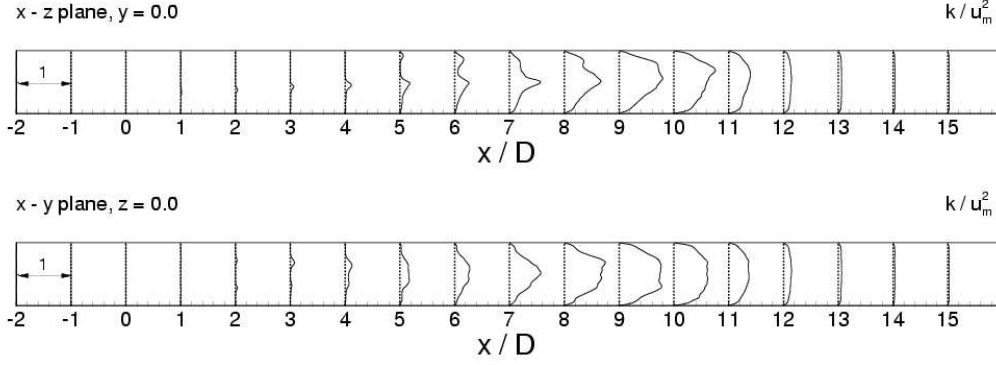


FIGURE 10. Turbulent kinetic energy (k) profiles, normalized by u_m^2 , for steady flow through the 75% eccentric stenosis at $Re = 1000$.

3.2.3. Energy spectra

Since transitional and turbulent flows contain a continuous spectrum of scales (i.e. with a wide separation of eddy sizes) it is usually worthwhile to characterize the nature of flow instabilities in terms of the frequency or spectral distribution of energy. The energy spectrum of the velocity signal is a measure of the frequency distribution of the energy contained within the turbulent fluctuations. To enable comparisons with previous experimental work (Cassanova & Giddens 1978; Deshpande & Giddens 1980; Ahmed & Giddens 1983b; Lu, Hui & Hwang 1983), we have defined the normalized spectrum, E^* , and Strouhal number, N_s , as

$$\begin{aligned} E^* &= \frac{E(f)u_j}{2\pi d}, \\ N_s &= \frac{2\pi f d}{u_j}, \end{aligned} \quad (3.1)$$

respectively. $E(f)$ is the frequency spectra of the normalized streamwise velocity fluctuations $(\frac{u'}{u_{r,m,s}})^2$, while f is the frequency of the fluctuation. As discussed by the above cited experimentalists, the mechanisms governing the formation of instabilities and transition to turbulence in the post-stenotic region are dominated by the characteristics of the constriction rather than the main vessel. To reflect this, we have used the mean velocity at the stenosis throat $u_j (= 4u_m)$ and minimum stenosis diameter $d (= 0.5D)$ as the characteristic velocity and length scale used to normalize the energy spectra in equation (3.1).

The frequency spectra $E(f)$ was computed by using Welch's overlapping averaged modified periodogram method (Welch 1967). The data was divided into four segments with 50% overlap, each section windowed with a cosine taper window (Hann window) to reduce leakage, and four modified periodograms were computed and averaged. The data sampling rate was 2kHz, corresponding to a Nyquist frequency of 1kHz.

Figure 11 shows normalized centerline disturbance energy spectra at various axial stations downstream of the stenosis throat. Motivated by the spectral analysis work by Mittal *et al.* (2003), the lines corresponding to $N_s^{-5/3}$ and N_s^{-7} have also been included in the figure. In turbulent flows, the $-5/3$ slope is associated with the range of wavenumbers in which the energy cascade is dominated by inertial transfer, *i.e.* the inertial subrange, while the N_s^{-7} variation characterizes the dissipation range where viscous forces dominate (Tennekes & Lumley 1972; Hinze 1975; Wilcox 1993).

Between $x = 2D$ and $4D$, energy is concentrated within a narrow frequency band,

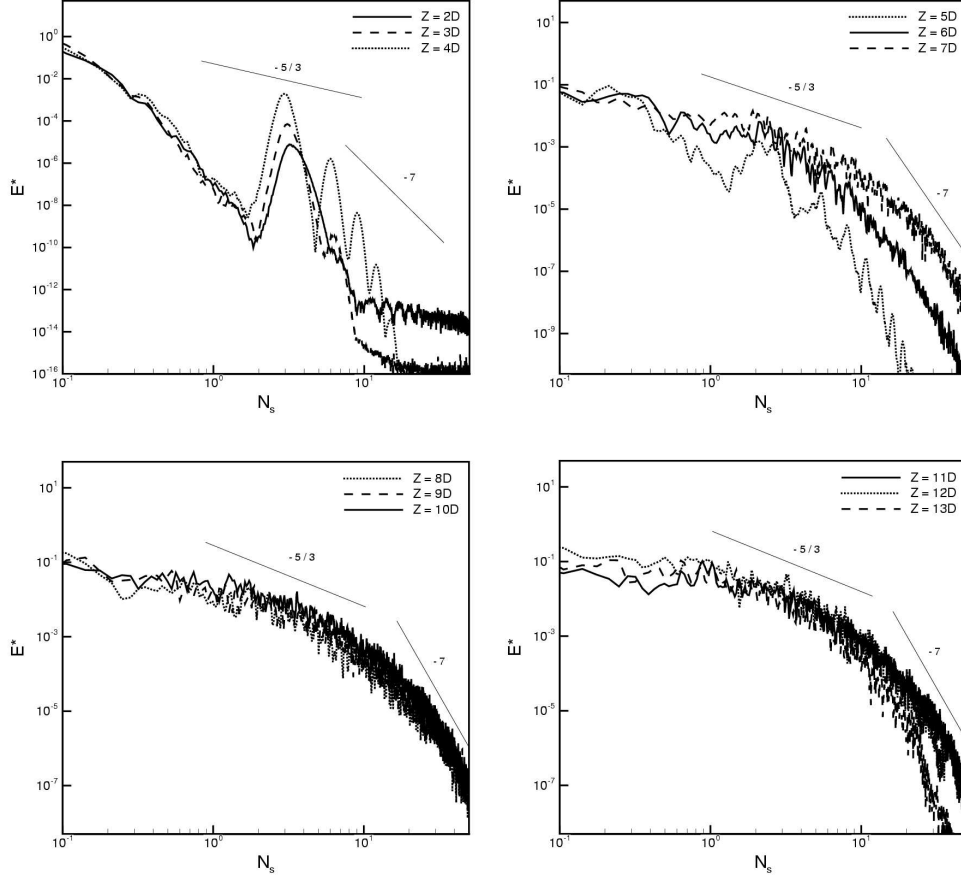


FIGURE 11. Normalized energy spectra of centerline streamwise velocity fluctuations, u' normalized by $u_{r.m.s.}$ for steady flow through the 75% eccentric stenosis at $Re = 1000$.

resulting in a peak at approximately $N_s = 3.14$. This indicates the passage of vortices through these locations at a relatively low vortex shedding frequency or Strouhal number (fd/u_j) of 0.5. The intensity of the spectral peak rises with increasing axial distance, indicating more energy transfer into the starting vortex structure. Multiple peaks seen at locations $x = 3D$ and $4D$ may be due to coalescing of the large-scale streamwise structures that form in the immediate downstream section. As these are convected downstream, they start to breakdown into smaller structures, resulting in the peaks at $x = 5D$ being dispersed over a broader range of frequencies with a slope of $-5/3$, corresponding to the inertial subrange. Farther downstream, at $x = 6D$ and beyond, the peaks characterizing discrete frequency phenomena are no longer present, and broadband spectra, characteristic of energy transfer between randomly distributed eddies in turbulent flows, are seen. At these locations, however, the range of frequencies comprising of the inertial subrange is fairly short, indicating that the energy cascade from the largest to the smallest eddies in the post-stenotic region does not occur over a large frequency range as in fully developed turbulent flows. The region between $x = 6D$ and $10D$ is most turbulent, with intensities dropping after $x = 10D$, confirming the observations in § 3.2.2. The range of frequencies over which the inertial subrange extends before rolling off to the $-10/3$ range becomes shorter as viscous effects start to dominate in the region $x > 10D$.

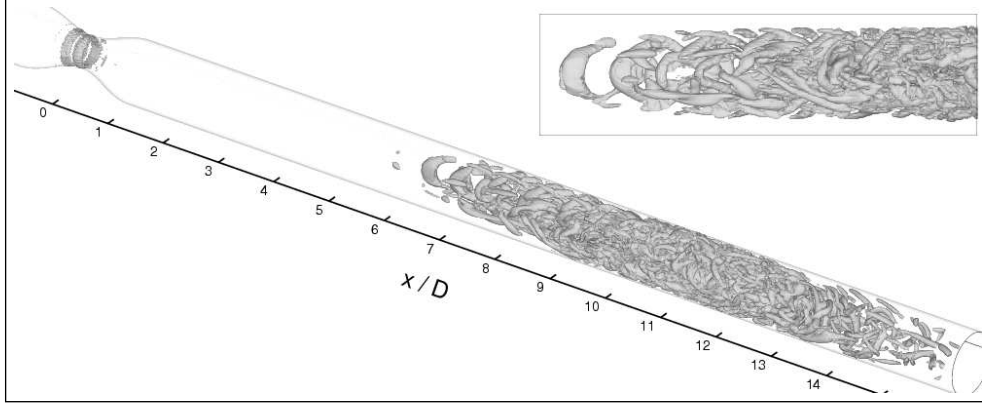


FIGURE 12. Instantaneous coherent structures (vortices) identified by using the isosurface corresponding to the negative contour -4.0 of the λ_2 criterion of Jeong & Hussain (1995), normalized by u_m/D , for steady flow through the 75% eccentric stenosis at $Re = 1000$. The inset shows a close-up view of the structures in the region $6D \leq x \leq 10D$.

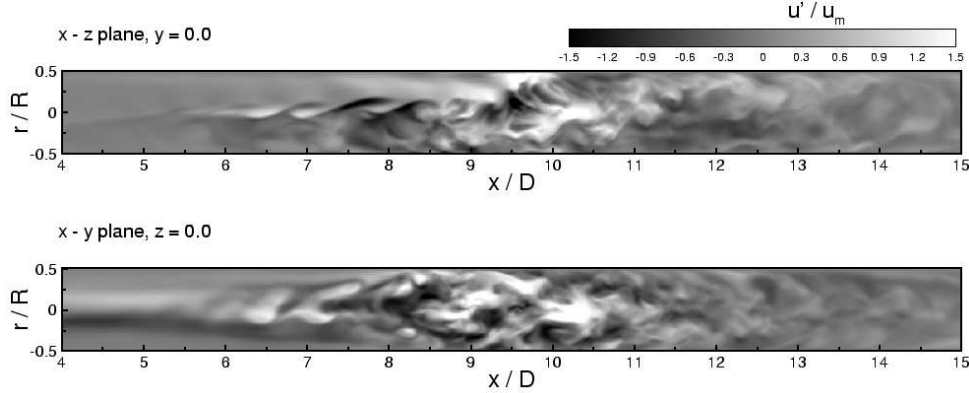


FIGURE 13. Instantaneous contours of streamwise velocity fluctuations u'/u_m , in the post-stenotic turbulent region for steady flow through the 75% eccentric stenosis at $Re = 1000$.

3.2.4. Turbulence structure

Instantaneous coherent structures, shown in figure 12 and clearly identified by isosurfaces of a negative contour of the λ_2 criterion of Jeong & Hussain (1995), together with contours of streamwise velocity fluctuations in figure 13, give an appreciation of the nature of turbulent breakdown in the post-stenotic flowfield. In the region between $x = 6D$ and $8D$, an array of streamwise vortices start to form. These vortices extend over an axial length of approximately half the main vessel diameter and closely resemble the hairpin vortices observed by Klebanoff, Tidstrom & Sargent (1962) in their seminal investigations of laminar-turbulent transition in boundary layers. The instability that propagates along the shear layer in the form of a wave-like roll-up, similar to the Kelvin-Helmholtz instability associated with highly inflectional velocity profiles in typical shear flows, is clearly highlighted by contours of streamwise velocity fluctuations. In the region beyond $x = 8D$, the streamwise vortices, deemed to play an important role in pipe flow transition by previous investigators (Eliahou *et al.* 1998; Shan *et al.* 1999; Han *et al.* 2000) by rendering the flow unstable to three-dimensional disturbances, instigate abrupt turbu-

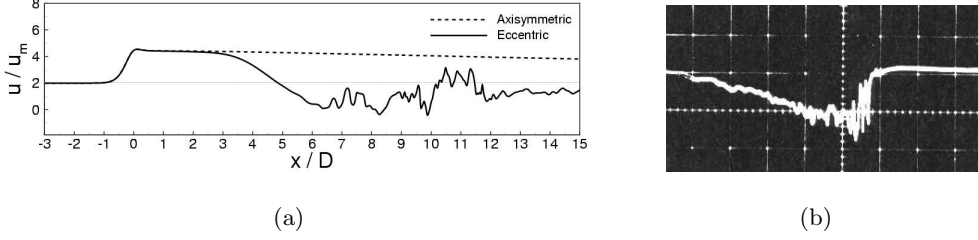


FIGURE 14. (a) Variation of instantaneous streamwise velocity u/u_m , along the centerline of the vessel for steady flow through the 75% axisymmetric and eccentric stenosis models at $Re = 1000$. (b) A time trace of streamwise velocity (along the centerline) associated with a turbulent puff, obtained for pipe flow at $Re = 2360$ (Wynanski & Champagne 1973).

lent breakdown. This gives rise to a turbulent spot that occupies the entire cross-section between $x \approx 9D$ and $12D$. The turbulent statistics and energy spectra presented in the previous sections indicate that turbulence intensity levels are highest within this spot.

Instantaneous streamwise velocity variations along the vessel axis are in effect the signatures left by the turbulent structures. In figure 14(a) they are presented along with corresponding results for the laminar, axisymmetric case at the same Reynolds number. The gradual deficit of streamwise velocity along the centerline after $x \approx 3D$ is apparent, as the flow transitions from a laminar, jet-like velocity profile to a more uniform turbulent profile, as a result of which the velocity close to the wall will rise. The region of the turbulent spot is coincident with streamwise velocity fluctuations that increase in intensity close to the trailing edge of the spot. After $x \approx 12D$, the velocity starts to increase while the fluctuation levels drop. Motivated by the recent study of spatially localized structures in pipe flow (Priymak & Miyazaki 2004), we compared these results with those associated with a turbulent "puff". Puffs were first reported by Wynanski & Champagne (1973) and Wynanski *et al.* (1975) in their early investigations of pipe flow transition at Reynolds numbers between 2000 and 2700. A characteristic trace of streamwise velocity along the pipe centerline, corresponding to the location of a puff, obtained by Wynanski *et al.* (1975) at a transitional Reynolds number of 2400 is shown in figure 14(b). The gradual velocity drop along the leading edge of the puff, followed by increasing turbulence intensity in the interior, closely resembles the velocity traces for the eccentric case. However, the trailing interface of the spot formed in the current simulations is not as distinct as in a typical puff, with the sharp growth in velocity at the trailing edge of the puff, as it regains its normal laminar value, not quite as visible in figure 14(a). Instead, there is an engulfment of laminar and turbulent fluid after $x \approx 11D$. The λ_2 structures in figure 12 also indicate the presence of weak streamwise structures in this region, which contribute to this mixing process as relaminarization progresses. However, centerline velocities in the region beyond $x = 12D$, downstream of the turbulent spot, are lower than their laminar counterparts, indicating that complete relaminarization does not occur within the length of the vessel considered for this study.

3.3. Wall shear stress

Figure 15(a) shows wall shear stress (WSS) magnitude variations across the entire vessel for the axisymmetric case at $Re = 500$. WSS levels increase from upstream values by more than a factor of thirty at the throat, as the fluid accelerates through the constriction, a value which compares reasonably to the measurements of Ahmed & Giddens (1983a), who found WSS at the throat to exceed upstream levels by a factor of twenty-four.

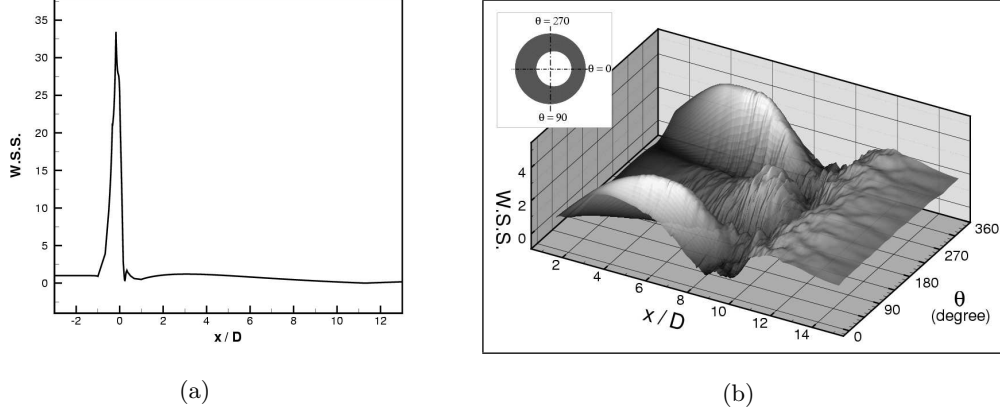


FIGURE 15. (a) Axial variation of wall shear stress (WSS) magnitude for steady flow through the 75% axisymmetric stenosis at $Re = 500$. (b) Axial and circumferential variation of time-averaged WSS magnitude in the post-stenotic region ($1D \leq x \leq 15D$) for steady flow through the 75% eccentric stenosis at $Re = 1000$. WSS levels have been normalized by the WSS upstream of the stenosis in both plots.

Subsequently, WSS levels return to their upstream values within the diverging section of the stenosis. The shear stress is actually negative along the reverse flow regions that form immediately downstream of the stenosis, though this is not evident from the results because only WSS magnitudes are shown.

Transition to turbulence in the post-stenotic flowfield for the eccentric model, at $Re = 1000$, results in large axial and circumferential variations in wall shear stress, as is readily apparent from figure 15(b). Only WSS levels in the post-stenotic region $x \geq 1D$ are shown, since the flow upstream and within the throat is almost identical to the flow predicted for the axisymmetric model, with the same large increase in stress at the throat, followed by a rapid drop. Immediately downstream of the stenosis, WSS levels are almost four times higher than upstream levels along the side of the vessel toward which the jet is initially deflected, while the opposite wall, between $\theta = 90$ and 270 in the figure, experiences levels lower than its upstream counterpart as a result of flow separation along this side. However, WSS levels in this region start to increase after $x \approx 6D$ with the advent of transition, eventually becoming as large as twice upstream levels when the flow completely breaks down into turbulence, at $x \approx 9D$. Large axial and circumferential gradients of WSS exist in the turbulent region, but these start to decrease after the trailing edge of the turbulent puff, discussed in the previous section. Shear stress magnitudes increase to almost one-half times upstream levels in the far downstream region $x > 12D$.

3.4. Comparison with previous studies

In the case of the axisymmetric stenosis, the simulations predict a completely stable and axisymmetric post-stenotic flowfield at both $Re = 500$ and 1000 . These results are unlike the observations made by Ahmed & Giddens (1983a,b) in their experiments, in which the post-stenotic region was completely laminar only at $Re = 250$. As the Reynolds number was increased to 500 , they observed that the shear layer exhibited periodic discrete frequency oscillations near the trailing edge of the recirculation region. At $Re = 1000$, vortex shedding at a discrete frequency was observed before $x = 4D$, after

which the flow transitioned into turbulence. The occurrence of transition downstream of the shear layer can result in a shifting of the reattachment point from that observed for a purely laminar flowfield. This may explain the differences between the computed and measured velocity profiles at $Re = 500$, shown in figure 6, especially at downstream locations close to the reattachment zone, $4D \leq x \leq 6D$. The experimental profiles in this region exhibit increased bluntness, while their computed counterparts maintain a jet-like character throughout. In general, as the Reynolds number increases, the transition region tends to move upstream, with the reattachment zone no longer as well defined as at lower Reynolds numbers. This phenomenon was clearly evident in our eccentric model simulations at $Re = 1000$, when transition to turbulence resulted in early flow reattachment. At $Re = 1000$, Ahmed & Giddens (1983b) observed discrete frequency vortex shedding at $x = 2.5D$ and intense turbulence (with $u_{r.m.s.}/u_m$ exceeding 70%) in the shear layer at $x = 4D$, a post-stenotic flowfield quite different from the laminar flowfield computed in this study at the same Reynolds number for the axisymmetric model.

As seen in § 3.2, an eccentricity of $0.05D$ at the stenosis throat was unable to trigger sustained disturbances, and the post-stenotic flowfield remained laminar throughout at $Re = 500$. At the higher Reynolds number of 1000, however, the geometric perturbation resulted in the flow transitioning to turbulence after $x = 6D$, as demonstrated by turbulent statistics and broadband energy spectra presented in § 3.2.2 and § 3.2.3. In spite of the geometric variation between our eccentric stenosis and the experimental axisymmetric model, the behavior of the flow in the post-stenotic region as it transitions into turbulence was markedly similar to the observations by Ahmed & Giddens (1983a) at the same Reynolds number. In both cases, as transition occurred, instabilities propagated along the shear layer, and turbulent energy was highest within it before being redistributed across the entire cross-section. The fact that transition to turbulence occurred earlier in the experiments, at $x = 4D$, could perhaps be attributed to instabilities arising from upstream noise, a factor that was absent in the current simulations.

With the same axisymmetric model, Ahmed & Giddens (1983a) measured the normalized centerline energy spectrum of streamwise velocity fluctuations, u' , similar to the computed spectra presented in the previous section. The experimentalists found that at $x = 1.5D$, the spectrum displayed a narrow peak at $N_s = 4.2$ followed by a broader peak at $N_s = 2.3$ farther downstream at $x = 2.5D$. Spectra at $x = 4D$ and $6D$ were characteristic of broadband turbulence, with no evidence of discrete frequency phenomena. The spectra shown in figure 11 for the eccentric case at $Re = 1000$ is consistent with these results in that the spectral peak at $x = 2D$ is at $N_s = 3.3$ and it shifts downward to about $N_s = 3.0$ at $x = 4D$ before dispersing into broadband spectra farther downstream. Also, the intensity of the spectral peak increased with axial distance, indicating more energy transfer into the starting vortex structure.

In an earlier study, Cassanova & Giddens (1978) analyzed flowfields downstream of both sharp-edged and axisymmetric contoured occlusions of varying degrees. The latter was generated by intersecting circular arcs, unlike the cosine wave used to generate the smooth stenosis in this study. For steady inlet flow at $Re = 635$, with a plug-shaped inlet velocity profile rather than a fully developed one, they observed that the 75% sharp-edged occlusion produced a set of small vortices that disintegrated before the stenotic jet expanded to meet the wall. However, the contoured occlusion produced a large-scale flow instability downstream of the stenosis, which appeared to break up upon interaction with the tube wall at the reattachment location, quite similar to the large streamwise structure that broke down into small-scale structures close to the reattachment zone at $Re = 1000$ in our eccentric model. Non-dimensional energy spectrum correlations by

the experimentalists indicated that the contoured occlusion showed spectral peaks at Strouhal numbers ($St = fd/u_j$) in the range $0.5 - 0.6$ at axial locations between $x = 1D$ and $3.125D$. The current results match these correlations well, with the spectral peaks in figure 11 occurring between $fd/u_j = 0.53$ and 0.48 at axial locations $x = 2D$ and $4D$, respectively.

The results obtained here are also consistent with the recent stability analysis studies of steady and pulsatile axisymmetric stenotic flows by Sherwin & Blackburn (2004). They observed that flow undergoes a Coanda-type wall attachment with jet deflection away from the axis of symmetry when a small perturbation flow component is added to an unstable steady base flow. Following saturation of this combination, the flow undergoes local transition to turbulence at a critical Reynolds number of 688, with the onset of turbulent breakdown propagating up to $x \approx 4D$. In the current simulations, in the presence of a geometric perturbation at the stenosis, transition to turbulence was triggered only after increasing the Reynolds number from 500 to 1000.

4. Conclusions

Direct numerical simulations of steady flow through smoothly contoured stenosed tubes with a maximum area reduction of 75% have been carried out. At inlet Reynolds numbers of 500 and 1000, DNS predicts a laminar flowfield downstream of an axisymmetric stenosis model. At $Re = 500$, the numerics agree with previous experimental measurements immediately downstream of the stenosis, but further downstream, after about four vessel diameters from the stenosis throat ($x \approx 4D$), the experiments recorded disturbed flow (with transition to turbulence occurring at $Re = 1000$) and consequently, early reattachment.

Symmetry breaking in our study was accomplished via a geometric perturbation in the form of a stenosis eccentricity, 5% of the main vessel diameter at the throat, a relevant addition in that real-life stenoses are more likely to be eccentric rather than axisymmetric. Stenosis eccentricity causes the jet to deflect towards the side of the eccentricity, but at $Re = 500$, the flow remained laminar. However, at a high enough inlet Reynolds number of 1000, jet breakdown occurred and the post-stenotic flowfield transitioned into localized turbulence. Low frequency vortex shedding, indicated by velocity spectra, was found to take place in the region between the throat and $x = 4D$, with more energy transfer into the vortices as the distance from the stenosis increased, the results matching well with experimental spectral correlations. Turbulence statistics indicated the presence of streamwise velocity fluctuations in this immediate downstream region but these are most likely due to the wave-like motion of the stenotic jet, rather than turbulence. The lack of coherent structures and turbulent kinetic energy, as well as the monochromatic nature of the spectra at these locations supports this conclusion. As flow transitioned into turbulence after $x \approx 5D$, the spectra started to take on a more broadband nature, achieving a $-5/3$ slope that is typical of turbulent flows. The transition process was accompanied by streamwise vortices that broke up to form a localized turbulent spot with large *r.m.s.* velocity and turbulent energy levels. The turbulent spot, comparable to turbulent puffs observed in pipe flow transition, was found to occupy the entire vessel cross-section between $x \approx 9D$ and $12D$, downstream of which the turbulent fluctuations and energy levels rapidly decayed and flow relaminarized. Broadband spectra confirmed that the flow within the spot was indeed turbulent.

Wall shear stress magnitudes at the stenosis throat were found to exceed upstream levels by more than a factor of thirty. The immediate post-stenotic section was characterized by low WSS levels, as a result of flow separation along the vessel walls. Transition

to turbulence in the case of the eccentric stenosis model was manifested in large temporal and spatial (both axial and circumferential) variations in WSS levels and magnitudes within the turbulent zone were almost three times higher than those found upstream of the stenosis.

The detailed analysis presented here, of steady flow through idealized stenosis models, at physiologically relevant Reynolds numbers, provides a fundamental understanding of the complex flowfield that may arise downstream of a clinically significant stenosis, as well as its impact on an important hemodynamic parameter such as wall shear stress. The steady flow analysis also serves as a suitable precursor to analysing the more physiologically realistic pulsatile flow. As Part 2 of this study (Varghese, Frankel & Fischer 2005) will go on to show, the flow features arising as a result of a stenosis, such as separation, reattachment, recirculation and strong shear layers, as observed here, combine with flow pulsatility to produce periodic transition to turbulence and subsequent relaminarization of post-stenotic flow.

REFERENCES

- ABDALLAH, S. A. & HWANG, N. H. C. 1988 Arterial stenosis murmurs: An analysis of flow and pressure fields. *J. Acoust. Soc. Am.* **83**, 318–334.
- AHMED, S. A. & GIDDENS, D. P. 1983a Velocity measurements in steady flow through axisymmetric stenoses at moderate Reynolds number. *J. Biomech.* **16**, 505–516.
- AHMED, S. A. & GIDDENS, D. P. 1983b Flow disturbance measurements through a constricted tube at moderate Reynolds numbers. *J. Biomech.* **16**, 955–963.
- AHMED, S. A. & GIDDENS, D. P. 1984 Pulsatile poststenotic flow studies with laser Doppler anemometry. *J. Biomech.* **17**, 695–705.
- BATHE, M. & KAMM, R. 1999 A fluid-structure interaction finite element analysis of pulsatile blood flow through a compliant stenotic artery. *J. Biomech. Eng.* **121**, 361–369.
- BERGER, S. & JOU, L.-D. 2000 Flows in stenotic vessels. *Annual Rev. Fluid Mechanics* **32**, 347–382.
- BUCHANAN JR., J., KLEINSTREUER, C. & COMER, J. 2000 Rheological effects on pulsatile hemodynamics in a stenosed tube. *Comp. and Fluids* **29**, 695–724.
- CASSANOVA, R. A. & GIDDENS, D. P. 1978 Disorder distal to modeled stenoses in steady and pulsatile flow. *J. Biomech.* **11**, 441–453.
- CLARK, C. 1980 The propagation of turbulence produced by a stenosis. *J. Biomech.* **13**, 591–604.
- DESHPANDE, M. D. & GIDDENS, D. P. 1980 Turbulence measurements in a constricted tube. *J. Fluid Mech.* **97**, 65–89.
- DEVILLE, M. O., FISCHER, P. F. & MUND, E. H. 2002 *High-Order Methods for Incompressible Fluid Flow*. Cambridge University Press.
- ELIAHOU, S., TUMIN, A. & WYGNANSKI, I. 1998 Laminar-turbulent transition in Poiseuille pipe flow subjected to periodic perturbation emanating from the wall. *J. Fluid Mech.* **361**, 333–349.
- FISCHER, P. F. 1997 An overlapping Schwarz method for spectral element solution of the incompressible Navier-Stokes equations. *J. Comp. Phys.* **133**, 84–101.
- FISCHER, P. F., KRUSE, G. & LOTH, F. 2002 Spectral element methods for transitional flows in complex geometries. *J. Scientific Computing* **17**, 81–98.
- FISCHER, P. F. & MULLEN, J. 2001 Filter-based stabilization of spectral element methods. *Comptes Rendus de l'Academie des sciences Paris, t. 332, - Serie I - Analyse numerique* 265–270.
- FREDBERG, J. J. 1974 Origin and character of vascular murmurs: Model studies. *J. Acoust. Soc. Am.* **61**, 1077–1085.
- HAN, G., TUMIN, A. & WYGNANSKI, I. 2000 Laminar-turbulent transition in Poiseuille pipe flow subjected to periodic perturbation emanating from the wall. Part 2. Late stage of transition. *J. Fluid Mech.* **419**, 1–27.

- HE, S. & JACKSON, J. 2000 A study of turbulence under conditions of transient flow in a pipe. *J. Fluid Mech.* **408**, 1–38.
- HINZE, J. O. 1975 *Turbulence*. McGraw-Hill.
- JEONG, J. & HUSSAIN, F. 1995 On the identification of a vortex. *J. Fluid Mech.* **285**, 69–94.
- KHALIFA, A. M. A. & GIDDENS, D. P. 1981 Characterization and evolution of post-stenotic flow disturbances. *J. Biomech.* **14**, 279–296.
- KIM, B. M. & CORCORAN, W. H. 1974 Experimental measurements of turbulence spectra distal to stenoses. *J. Biomech.* **7**, 335–342.
- KLEBANOFF, P. S., TIDSTROM, K. D. & SARGENT, L. M. 1962 The three-dimensional nature of boundary layer instability. *J. Fluid Mech.* **12**, 1–34.
- KU, D. N. 1997 Blood flow in arteries. *Ann. Rev. Fluid Mech.* **29**, 399–434.
- LIEBER, B. B. & GIDDENS, D. P. 1988 Apparent stresses in disturbed pulsatile flows. *J. Biomech.* **21**, 287–298.
- LIEBER, B. B. & GIDDENS, D. P. 1990 Post-stenotic core flow behavior in pulsatile flow and its effects on wall shear stress. *J. Biomech.* **23**, 597–605.
- LU, P. C., GROSS, D. R. & HWANG, N. H. C. 1980 Intravascular pressure and velocity fluctuations in pulmonic arterial stenosis. *J. Biomech.* **13**, 291–300.
- LU, P. C., HUI, C. N. & HWANG, N. H. C. 1983 A model investigation of the velocity and pressure spectra in vascular murmurs. *J. Biomech.* **16**, 923–931.
- LUSIS, A. J. 2000 Atherosclerosis. *Nature* **407**, 233–241.
- MADAY, Y., PATERA, A. T. & RØNQUIST, E. M. 1990 An operator-integration-factor splitting method for time-dependent problems: Application to incompressible fluid flow. *J. Scientific Computing* **5**, 263–292.
- MALLINGER, F. & DRIKAKIS, D. 2002 Instability in three-dimensional unsteady stenotic flows. *Int. J. Heat Fluid Flow* **23**, 657–663.
- MITTAL, R., SIMMONS, S. P. & NAJJAR, F. 2003 Numerical study of pulsatile flow in a constricted channel. *J. Fluid Mech.* **485**, 337–378.
- OJHA, M., COBBOLD, C., JOHNSTON, K. & HUMMEL, R. 1989 Pulsatile flow through constricted tubes: An experimental investigation using photochromic tracer methods. *J. Fluid Mech.* **13**, 173–197.
- PRIYMAK, V. G. & MIYAZAKI, T. 2004 Direct numerical simulation of equilibrium spatially localized structures in pipe flow. *Phys. Fluids* **16**, 4221–4234.
- RYVAL, J., STRAATMAN, A. G. & STEINMAN, D. A. 2004 Two-equation turbulence modeling of pulsatile flow in a stenosed tube. *J. Biomech. Eng.* **126**, 625–635.
- SCOTTI, A. & PIOMELLI, U. 2001a Numerical simulation of pulsating turbulent channel flow. *Phys. Fluids* **13**, 1367–1384.
- SCOTTI, A. & PIOMELLI, U. 2001b Turbulence models in pulsating flow. AIAA Paper 01-0729.
- SHAN, H., MA, B., ZHANG, Z. & NIEUWSTADT, F. T. M. 1999 Direct numerical simulation of a puff and a slug in transitional cylindrical pipe flow. *J. Fluid Mech.* **387**, 39–60.
- SHERWIN, S. J. & BLACKBURN, H. M. 2004 Three-dimensional instabilities of steady and pulsatile axisymmetric stenotic flows. *Submitted to J. Fluid Mech.*
- STROUD, J., BERGER, S. & SALONER, D. 2000 Influence of stenosis morphology on flow through severely stenotic vessels: Implications for plaque rupture. *J. Biomech.* **33**, 443–455.
- TANG, D., YANG, J., YANG, C. & KU, D. 1999 A nonlinear axisymmetric model with fluid-wall interactions for steady viscous flow in stenotic elastic tubes. *J. Biomech. Eng.* **121**, 494–501.
- TENNEKES, H. & LUMLEY, J. L. 1972 *A First Course in Turbulence*. MIT Press.
- VARGHESE, S. S. & FRANKEL, S. H. 2003 Numerical modeling of pulsatile turbulent flow in stenotic vessels. *J. Biomech. Eng.* **125**, 445–460.
- VARGHESE, S. S., FRANKEL, S. H. & FISCHER, P. F. 2005 Direct numerical simulation of stenotic flows, Part 2: Pulsatile flow. *Preprint*.
- WELCH, P. D. 1967 The use of fast Fourier transform for the estimation of power spectra: A method based on time averaging over short modified periodograms. *IEEE Trans. Audio Electroacoustics*, vol. AU-15, pp. 70–73.
- WILCOX, D. 1993 *Turbulence modeling for CFD*. La Cañada, California, CA: DCW Industries.

- WINTER, D. C. & NEREM, R. M. 1984 Turbulence in pulsatile flows. *Ann. Biomed. Eng.* **12**, 357–369.
- WOMERSLEY, J. R. 1955 Method for the calculation of velocity, rate of flow and viscous drag in arteries when the pressure gradient is known. *J. Physiology* **127**, 553–563.
- WOOTTON, D. M. & KU, D. N. 1999 Fluid mechanics of vascular systems, diseases, and thrombosis. *Annu. Rev. Biomed. Eng.* **1**, 299–329.
- WYGNANSKI, I. J. & CHAMPAGNE, F. H. 1973 On transition in a pipe. Part 1. The origin of puffs and slugs and the flow in a turbulent slug. *J. Fluid Mech.* **59**, 281–335.
- WYGNANSKI, I. J., SOKOLOV, M. & FRIEDMAN, D. 1975 On transition in a pipe. Part 2. The equilibrium puff. *J. Fluid Mech.* **69**, 283–304.
- YOUNG, D. F. 1979 Fluid mechanics of arterial stenosis. *J. Biomech. Eng.* **101**, 157–173.
- YOUNG, D. F. & TSAI, F. Y. 1979a Flow characteristics in models of arterial stenoses - I steady flow. *J. Biomech. Eng.* **6**, 395–410.
- YOUNG, D. F. & TSAI, F. Y. 1979b Flow characteristics in models of arterial stenoses - II unsteady flow. *J. Biomech. Eng.* **6**, 547–559.

The submitted manuscript has been created by the University of Chicago as Operator of Argonne National Laboratory ("Argonne") under Contract No. W-31-109-ENG-38 with the U.S. Department of Energy. The U.S. Government retains for itself, and others acting on its behalf, a paid-up, nonexclusive, irrevocable worldwide license in said article to reproduce, prepare derivative works, distribute copies to the public, and perform publicly and display publicly, by or on behalf of the Government.